J. Fluid Mech. (1995), *vol.* 289, *pp.* 51–82

Capillary–gravity and capillary waves generated in a wind wave tank: observations and theories

By XIN ZHANG

Scripps Institution of Oceanography, University of California, San Diego, La Jolla, CA 92093-0230, USA

(Received 29 July 1994 and in revised form 10 November 1994)

Short water surface waves generated by wind in a water tunnel have been measured by an optical technique that provides a synoptic picture of the water surface gradient over an area of water surface (Zhang & Cox 1994). These images of the surface gradient can be integrated to recover the shape of the water surface and find the two-dimensional wavenumber spectrum. Waveforms and two-dimensional structures of short wind waves have many interesting features: short and steep waves featuring sharp troughs and flat crests are very commonly seen and most of the short waves are far less steep than the limiting wave forms; waveforms that resemble capillary–gravity solitons are observed with a close match to the form theoretically predicted for potential flows (Longuet-Higgins 1989); capillaries are mainly found as parasitics on the downwind faces of gravity waves, and the longest wavelengths of those parasitic capillaries found are less than 1 cm; the phenomenon of capillary blockage (Phillips 1981) on dispersive freely travelling short waves is also observed. The spectra of short waves generated by low winds show a characteristic dip at the transition wavenumber between the gravity and capillary regimes, and the dip becomes filled in as the wind increases. The spectral cut-off at high wavenumbers shows a power law behaviour with an exponent of about minus four. The wavenumber of the transition from the dip to the cut-off is not sensitive to the change of wind speed. The minus fourth power law of the extreme capillary wind wave spectrum can be explained through a model of energy balances. The concept of an equilibrium spectrum is still useful. It is shown that the dip in the spectrum of capillary–gravity waves is a result of blockage of both capillary–gravity wind waves and parasitic capillary waves.

1. Introduction

Very short wind waves are important because they affect energy, momentum and material fluxes through the sea surface. Here we use the term short surface waves to refer to capillary and gravity–capillary surface waves with wavelengths in the range of a millimetre to several centimetres. One indication of the importance of short waves arises from their steepness. Gravity waves have generally moderate or small slopes, but the slopes of capillary waves can be unlimited. Because of their steepness the area of the air–sea interface is significantly increased. The roughness of the sea surface exposed to wind is an important parameter affecting turbulence in the air and sea boundary layers, the transfer of momentum and gases across the sea surface, and the development of wind waves. An understanding of short waves is an important aspect of interpreting the microwave remove sensing images of the sea surface. These methods depend on

electromagnetic scattering and radiation in the L-, X- or K-band where the microwave wavelengths are comparable to the scale of the short waves. The acoustic behaviour of bubbles entrained in water is another important factor.

Nonlinearity in finite-amplitude gravity surface waves of permanent form leads to sharp crests and flat troughs (Stokes 1880). Wilton (1915) made a pioneering study of nonlinear gravity–capillary waves. Later Crapper (1957) predicted that deep-water capillary waves in an inviscid, irrotational flow have the profiles characterized by deep troughs and broad flat crests. This prediction has received some experimental support from laboratory studies by Schooley (1958). In the limiting form of a Crapper capillary, the free surface adjacent to the trough becomes vertical and then finally curls around to pinch off a bubble of 'air'. For gravity–capillary waves no exact solutions are known, but through numerical calculations, Schwartz & Vanden-Broeck (1979) and Hogan (1980) showed that short waves are capillary-like in nature. The subject matter of all these studies was a periodic train of waves.

Longuet-Higgins (1989) suggested the existence of solitary waves (similar to those of Russell on shallow water) for capillary–gravity waves on deep water. To the best of my knowledge, these capillary–gravity solitary waves have not yet been observed. Capillary–gravity solitons are predicted to have a sharp trough similar to periodic capillary waves of finite amplitude, and in the limiting form, they enclose an air bubble.

Under the influence of wind, there is a wind-drift shear layer just below the water surface. Wu (1968) measured a surface drift of about 4% of the mean wind, and a thickness of 3–5 mm. The wind drift can change the waveform of very short waves to an unknown extent. It has been shown (Simmen & Saffman 1985) that a uniform vorticity field can change the waveform of gravity waves.

Parasitic capillary waves on the downwind faces of gravity waves propagate as groups (Cox 1958). The linear theory of parasitic waves (Longuet-Higgins 1963) predicts that the wavelengths of parasitic capillaries decrease toward the trough of the long wave on which they ride, and the slopes of parasitic capillaries increase first then decrease owing to viscous damping as wavelengths decrease. However, it is observed that in the wind wave field (Schooley 1958; Ebuchi, Kawamura & Toba 1987), there is a steep surface dip at the upper end of parasitic capillaries near the long-wave crest. From fluid visualizations, Okuda, Kawai & Toba (1977) suggested the occurrence of a very strong vortical region at the crest of the gravity wave. Longuet-Higgins (1992) accounts for this phenomenon by including the vorticity introduced by steep capillary waves. Ebuchi *et al.* (1987) concluded from an observation of 'specular facets' of short wind waves that at a certain wind speed there is a streamwise streak structure on the rear face of long waves.

Short wind waves are generated by a number of mechanisms. Among these are turbulent pressure fluctuation in the air convected across the water surface (Phillips 1957; Plant & Wright 1977) and wave induced instability of the boundary layers in the air and water (Miles 1962; Valenzuela 1976; Kawai 1979). Capillary waves are also generated on the crests of steep gravity waves even in the absence of wind. Another important factor is the straining imposed on the capillaries as they propagate through the orbital velocity field of the gravity waves. This changes the steepness, wavelength, and dissipation of the capillaries (Phillips 1981; Longuet-Higgins 1987*a*).

The description of the chaotic gravity wave field as a random stochastic process also has a long history. It has been found that the second-order statistics, thus the wave spectrum, is useful for studying the wave energy balances. Hasselmann (1962, 1963) calculated the transfer of energy by nonlinear interactions among the components of gravity waves, a process that has been shown to be very important in the development

of the wind wave spectrum (Hasselmann *et al.* 1973 (JONSWAP)). The method has been extended to include gravity–capillary surface waves by Valenzuela & Laing (1972) and Holliday (1977). There are several models to describe different parts of the wind wave spectrum. Among these, the equilibrium range spectrum was developed for gravity wind waves at frequencies well above those of the energy peak. A simple form based on the limitation of waveforms by whitecapping was first proposed by Phillips (1958). Later Phillips (1985) provided a refined model that reflected dynamical insight into wave–wave interactions and energy input from the wind, and took into consideration the ideas developed by Toba (1973) and Kitaigorodskii (1983) as well as large amounts of new experimental data.

The time series of slopes of short wind waves have been measured for almost forty years since Cox (1958). The frequency spectrum derived from single-point measurements of waves provides features of short waves, but is unable to show the intrinsic frequency spectrum of short wind waves because Doppler shifting of short-wave components by orbital motion of underlying long waves distorts their frequencies. The wavenumber spectrum of the shortest waves, that is capillary waves, has only recently become available (Jähne & Riemer 1990). A new method (Zhang & Cox 1991, 1994) has been developed to measure the water surface gradient. With this new method it is possible to infer both the wavenumber spectrum and the spatial structure of the elevation of the water surface over a small, but useful area. The spectrum data show (Zhang 1994): at low wind speeds, there is a spectral dip in the capillary–gravity band that is filled in at higher wind speeds; after rising out of the dip, the spectrum decreases in the extreme capillary range as the minus fourth power of wavenumber; the widening of angular spreading of energy density spectra is not monotonic with increasing wavenumber. There is a local platform of minimum angular spreading in the spectral band of parasitic capillary waves.

Valenzuela & Laing (1972) explained the frequency spectral dip in the capillary–gravity band by a process involving the wave instability, but this model cannot explain why the dip fills in at high wind speeds and why the dip is much less pronounced at long fetch. On whether there is an equilibrium spectrum in the capillary range, Phillips (1966) remained cautious because of the complexity of shape of capillaries and viscous dissipation. Toba (1988) extended his similarity laws of the wind wave spectrum to include the surface tension. Jähne (1989) extended the equilibrium spectrum of short wind gravity waves to the capillary wave regime. Neither of these extensions to the wave spectrum fits the observed cutoff and this leads us to reconsider these extending theories.

In this paper, the methods of measuring surface and our experimental set-up are first outlined. The spectral data of short wind waves are summarized in §3. The observed characteristics of individual waveforms of steep short waves, soliton-like structures, and the two-dimensional structures of parasitic capillaries are described in some detail in §4. The rest of the paper is then focused on analysing and interpreting the observed properties of short wind waves especially on the wavenumber spectrum. Discussions about the influence of the straining of short waves by long-wave orbital velocity and wave–wave interactions among the short waves follows in §§5 and 6, respectively, with a focus on some interesting characteristics of capillary waves. It is shown that parasitic capillaries of wavelength larger than about 1 cm are unlikely to be developed. For short-wave groups, with a narrow band and a narrow directional spreading factor, interactions among a quartet of short waves are important and the energy fluxes among different wavenumbers are derived. In §7, we develop a model of the spectrum extending from the gravity–capillary dip through the capillary range based on the ideas

of equilibrium through energy balances. In §8, further evidence supporting the model and indications from the model is discussed.

2. Measuring short wind waves with a two-dimensional surface gradient detector

A novel optical method of measuring fluid surface gradient is developed and used to measure short wind waves. The principle of the method is simple. A fresnel lens is placed horizontally under the water surface far below the deepest troughs of gravity wind waves. On its focal plane below, there is an optical-scatter light-plane source. This plane is made of a large illuminated slide of a two-dimensional colour pattern. The lens transforms each point of light source on the focal plane into a beam of parallel rays propagating toward the water surface from below. The direction of each beam of parallel rays is determined by the position of the corresponding point on this focal plane. The colours of the light screen are different from point to point and so are the colours of beams of parallel rays that approach the water surface. Through this simple transform of geometric optics, a light source of which directions of emitting rays are colour coded is formed. The refraction rays of light across the fluid surface from below are observed by a 35 mm film camera far above the surface. The distance from the camera to the water surface is set to be much larger than the field of the camera view, so that the directions of the light rays entering the camera to form images on films can then be kept approximately the same. When the positions of the camera and the lens are all fixed, the colour of the entering rays to the camera from each point on the water surface varies only with the water surface slope of the corresponding point determined completely by Shell's refraction law. The fluid surface slopes (gradient) are thus mapped into the colour space so that the image of the fluid surface gradient can be recorded on a colour film. Colour images of the fluid surface are then digitized into a computer. The slopes of the fluid surface are estimated through the digital inverse colour mapping. Details about this water surface gradient detector and its calibration, noise filtering, conversion of image data to surface gradient and surface elevation, and its overall performance can be found in Zhang & Cox (1994).

Some features of this two-dimensional measurement technique are the following: wave surface elevations throughout the photographed area can be reconstructed by integrating the gradient data; the water area over which slopes can be measured is restricted by the size of the lens and its depth below the water surface; variations in the water surface elevation do not change the colour of the surface, therefore, the slope measurements are independent of the surface elevation; the method is effective even when the wavy water surface has as broad a spectral distribution as wind waves. In our measurements, waves with slope angles as large as 50° from the horizontal can be measured, and capillary waves with wavelengths as short as 0.3 mm are resolved.

Observations were carried out in the wind wave facility in the Hydraulics Laboratory of the Scripps Institution of Oceanography. The channel is closed at the top and is 2.4 m wide, 2.4 m deep and 44 m long. The channel is filled with fresh water to a depth of 1.2 m. A skimmer is placed at the downwind end of the tank to keep the surface clean by extracting contaminating surface films that tend to form on the water surface. Air enters the channel through a right-angle elbow nozzle and is drawn above the water by a suction fan beyond the downwind end of the channel. The resulting water waves are dissipated in an absorber at the downwind end of the channel. The gradient measuring apparatus is situated at a fetch of 24 m and has been used to study wave slopes generated at wind speeds in the range of 5 to 10 m s^{-1}. Wave energy spectra peak at wavelengths from 30 to 50 cm. Two resistance-type wave staffs and an anemometer

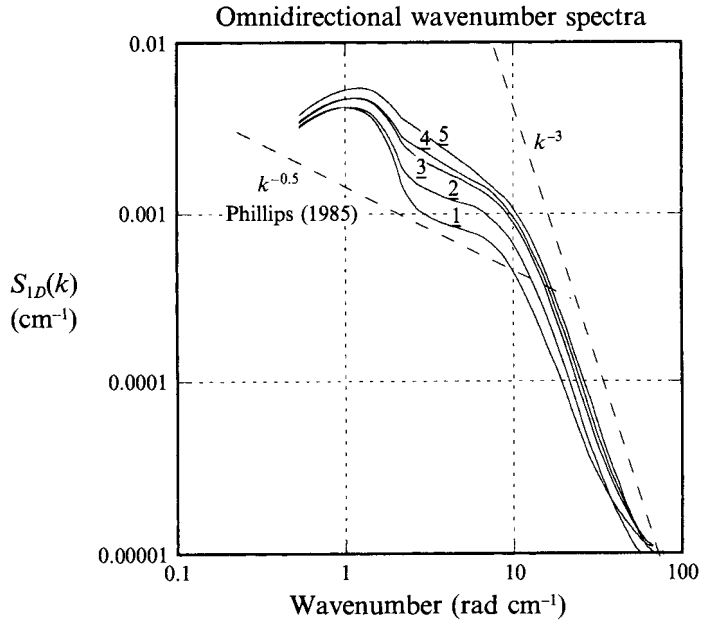

FIGURE 1. Wavenumber spectra of total slope at 5 different wind speeds with labels corresponding to the run number of table 1. The spectra have been integrated over all the directions.

placed downwind of the detector are used to measure long gravity waves and wind speeds. The friction velocity is derived from our measured wind profiles (using hot-film anemometry) in the channel under the assumption of a logarithmic boundary profile. These measured profiles are logarithmic within the turbulent boundary layer over the wavy water surface and linear within the interior of the channel air flow (Zhang 1994).

3. The wavenumber spectrum of short wind waves

From digital slope data derived from the colour photographic images, wavenumber spectra of the two orthogonal components of water slope $S_x(\boldsymbol{k})$ and $S_y(\boldsymbol{k})$ have been found at several wind speeds. The total slope spectrum $S(\boldsymbol{k})$ is defined as the sum of the two slope spectra. It is also the product of the wave height spectrum $\Psi(\boldsymbol{k})$ and the square of the wavenumber:

$$S(\boldsymbol{k}) = S_x(\boldsymbol{k}) + S_y(\boldsymbol{k}) = k_x^2\,\Psi(\boldsymbol{k}) + k_y^2\,\Psi(\boldsymbol{k}) = k^2\Psi(\boldsymbol{k}). \tag{3.1}$$

The slope spectra integrated over all directions,

$$S_{1D}(k) = \int S(\boldsymbol{k})\,k\,\mathrm{d}\theta \propto S(\boldsymbol{k})\,k,$$

are shown in figure 1 for the various wind speeds as listed in table 1. The details about the two-dimensional spectral data can be found in Zhang (1994). The widening of angular spreading of energy density spectra is not monotonic with increasing of wavenumber. There is a local platform of minimum angular spreading in the spectral band of parasitic capillary waves (see figures 12 and 13 of Zhang 1994).

The spectra $S(\boldsymbol{k})$ have other two distinct features, a dip in the capillary–gravity range and a cutoff of about the minus fourth power (minus third for $S_{1D}(k)$) in the extreme capillary range. (The departure from a power law for $k > 60$ rad cm^{-1} is due to the

Run number	Wind speed ($m\,s^{-1}$)	Friction velocity ($cm\,s^{-1}$)	Number of images	Number of blocks in each image	Number of independent taper windows	Degrees of freedom
1	5.9	40	64	3	8	1024
2	6.7	46	74	3	8	1184
3	7.8	53	76	3	8	1216
4	8.9	61	70	3	8	1120
5	9.7	66	35	3	8	560

TABLE 1. Summary of spectral data

system noise.) The dip is pronounced at very low wind speeds and is gradually filled in at higher wind speeds. The turning point from the dip to the steep decay slope on the spectra is not sensitive to the wind speed and, it is somewhere between 7 and 10 rad cm^{-1}. The spectra we measured are consistent with the classical data of frequency spectra of wave slopes by Cox (1958) at a fetch of 2.4 m that clearly show there is a dip in the capillary–gravity region at low wind speeds that is filled out at high wind speed and there is a characteristic decay slope of minus fourth to minus fifth frequency power law. The wavenumber spectral data measured by Jähne & Riemer (1990) at a fetch of 90 m do not show a clear dip in the capillary–gravity range and do show that there is a -2.5 wavenumber power law in the spectra of degree of saturation (defined as $S(\boldsymbol{k})k^2$) which is equivalent to a -4.5 power law of total slope spectrum $S(\boldsymbol{k})$.

Toba (1988) extended his similarity laws of the wind wave frequency spectrum to include the surface tension T ($T = T'/\rho$) by substituting for acceleration due to gravity g the effective acceleration $g_* = g + Tk^2$:

$$\Psi(\sigma) = \alpha g_* u_* \sigma^{-4}. \tag{3.2}$$

This is equivalent to a -2.5 power law for the total slope wavenumber spectrum of capillary waves. This model clearly cannot explain the experiment data.

Jähne (1989) extended the equilibrium spectrum of short gravity wind waves (Phillips 1985) to the gravity–capillary and capillary regimes by keeping the same energy balance terms but replacing triplets for quartets in the wave–wave interactions. This leads to the spectrum form:

$$\Psi(\boldsymbol{k}) = \beta f(\theta) u_*^2 k^{-5}, \tag{3.3}$$

which is equivalent to a -3 power law for the total slope wavenumber spectrum. This extension is unable to explain the experimental data in the dip or in the extreme cutoff regions.

There is an important scale in the spectrum. k_m is the wavenumber where both gravity and surface tension are equally important:

$$k_m = \left(\frac{g\rho}{T}\right)^{1/2} = 3.64\ (\text{rad cm}^{-1}). \tag{3.4}$$

Locally, three-wave interactions rather than four-wave interactions become important because of the concave nature of the dispersion relation. The overall effect of this triple wave interaction is to push energy toward higher and lower wavenumbers according to the calculation by Valenzuela & Laing (1972). This calculation suggests that there can be a dip in the capillary–gravity range of the wave spectrum but cannot explain why the dip is filled in at high wind speeds and our measured angular spreading of wavenumber spectra.

4. Wavy surface of very short wind waves

4.1. *General characters of capillary and capillary–gravity wind waves*

The theoretical predictions of waveforms of short waves are characterized by sharp troughs and flat crests for the finite-amplitude waves of potential flow fields. We have observed such forms qualitatively in steep and short wind waves, especially those with lengths less than two centimetres or so. Examples of short wind wave forms are shown in figure 2. The grey level of the wave image represents the magnitude of surface gradient. Three equal spaced profiles of the wave surface elevation along the wind direction are taken from the image. The vertical scaling of these wave profiles is exaggerated at a factor about 3:1. Waveforms and patterns we observed in the wind wave tank show a great variety. Steep slopes are always found to be in the troughs of very short waves. The steepest waves occur usually at the long-wave crest end of parasitic wavetrains or as individual soliton-like forms. Very short waves with lengths less than 1 cm exist at all different wind speeds and are mainly characterized as parasitic waves, while waves of several centimetre wavelengths increase in steepness more rapidly with the wind speed from almost none at low wind speed. The slopes of short waves of all ranges of wavelengths increase with the wind speed at different rates (see figure 12). The feature of a sharp trough does not frequently appear for those multicentimetre waves and usually there are shorter waves propagating with them near their troughs. Very steep short waves that exceed our measurable range (50°) can be found occasionally at low wind speeds and the number increases with the wind speed but is still quite limited. The 50° limit is most frequently exceeded in the first trough of parasitic waves at the long-wave crest end when the underlying gravity wave nearly breaks. Most short waves do not exceed this limit. This suggests that the assumption of infinitesimal amplitude and slope may still be used as a good approximation in the statistical sense in our wind speed range.

The short waves in wind fields can be categorized into two main classes by their appearance: parasitic capillary waves and short random waves. Parasitic capillaries on the downwind faces of gravity waves extract energy mainly from gravity weaves and are dissipated by viscosity, while we refer to random waves as those waves other than parasitic waves such as short waves generated directly by wind actions. All the short waves feel all the forces in reality. Parasitic capillaries are well organized. They are quasi-parallel to the long-wave crests and have a narrow directional spreading factor. Random waves exhibit a great variety of two-dimensional spatial patterns. There are few of them at very low wind speeds especially when underlying gravity waves are steep but as the wind picks up, they gradually increase. Their directional pattern is quite broad. These match the characters of observed wavenumber spectra described in §3 that the spectrum of capillaries has a narrower angular spreading and spectrum of capillary–gravity waves has a dip which is filled in at high wind speeds.

4.2. *Solitary waves of capillary–gravity type*

An important observed phenomenon is the isolated steep surface dips which resemble the Longuet-Higgins' soliton of capillary–gravity waves. The theoretical existence of this kind of soliton was first suggested on physical grounds by Longuet-Higgins (1988) and the waveforms of a family of them with the phase-speed c in the range of $0.926\,(gT/\rho)^{1/4} < c < 1.30\,(gT/\rho)^{1/4}$ were derived through an accurate numerical computation by Longuet-Higgins (1989). His theory predicted that the larger the slope of the solitary wave is, the slower its phase speed. The profile for $c = 0.926\,(gT/\rho)^{1/4}$ represents the critical case when the free surface touches itself and encloses a 'bubble'.

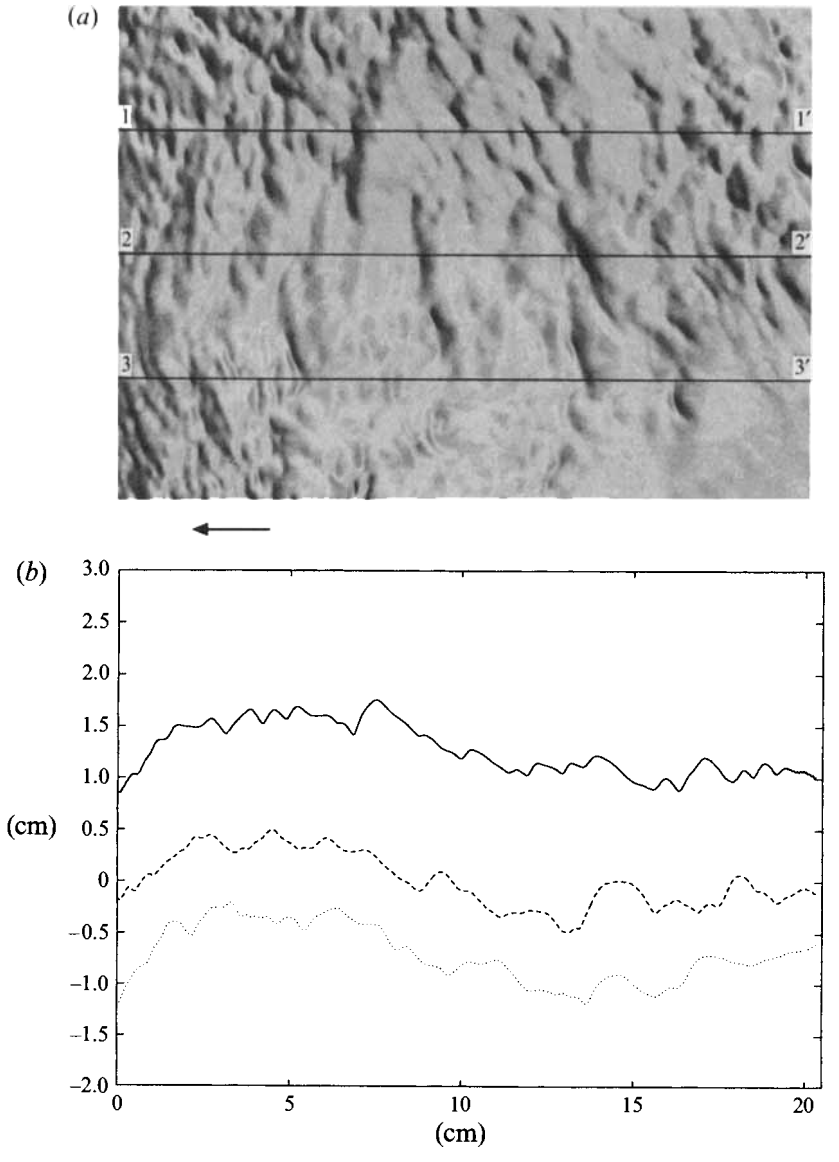

FIGURE 2. Examples of waveforms and structures of short wind waves with a fetch of 24 m. (*a*) A gradient image of wind wave field at a wind speed of 7.8 m s^{-1} (wave field of about 20 × 14 cm); (*b*) surface profiles along three horizontal sections of (*a*): ——, section 11′; – – –, section 22′; ·····, section 33′. Vertical adjustments are added to avoid overlapping the curves.

The corresponding maximum angles of inclination α_{max} of this group of 'depression' solitary waves are in the range of $1.712 > \alpha_{max} > 0.59$. Further numerical calculations of Vanden-Broeck & Dias (1992, hereinafter referred to as VBD) using a different numerical technique have verified the existence of the 'depression' solitary waves and have also found 'elevation' solitary waves. The soliton surface profiles of VBD suggest that, as the amplitude of the solitary waves is decreased, the waves spread out horizontally and develop more and more undulations. Recently, Longuet-Higgins (1993) has shown that in fact there exist solitons of arbitrarily small amplitude, and these are just a special type of envelope-soliton having a carrier wave of length

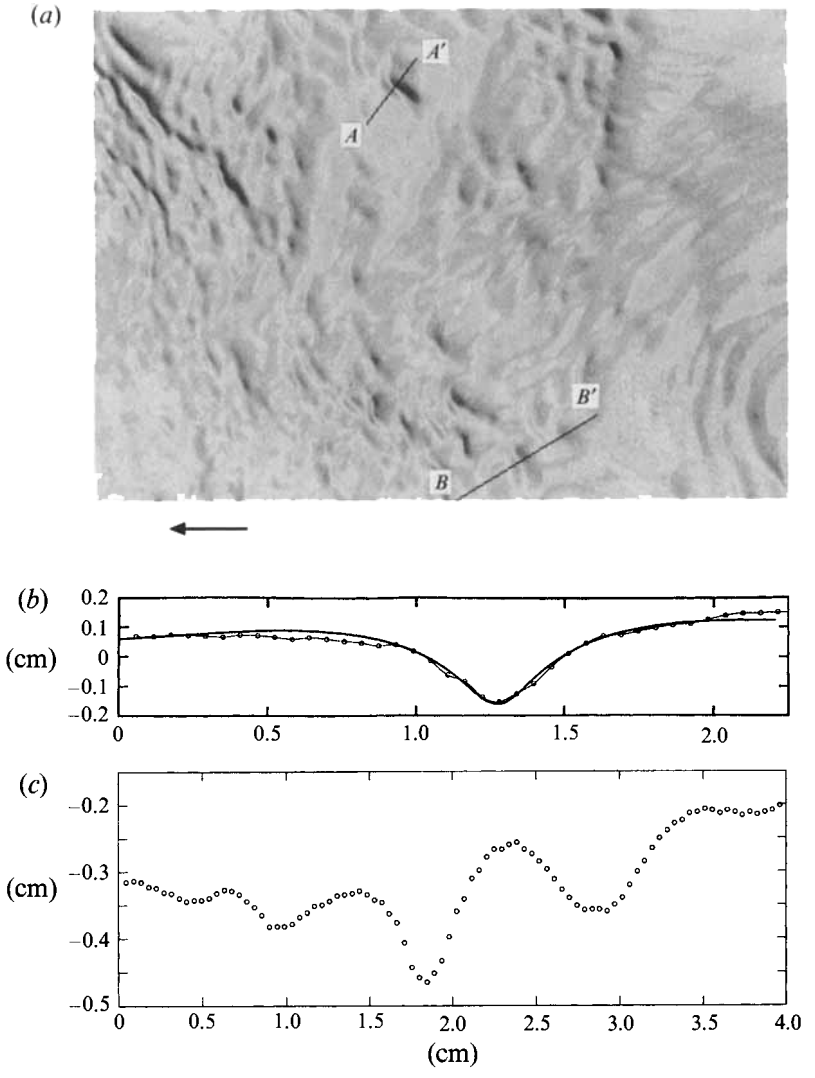

FIGURE 3. Solitary waves. (*a*) A gradient image of short wave field. Wind speed 5.9 m s^{-1} (wave field of 20 × 14 cm). (*b*) Waveform profile of section AA', the measured curve with circles matches with the solitary wave form of phase speed of $1.25(gT/\rho)^{1/4}$. (*c*) Waveform profile of section BB' which has multiple 'depressions'.

$2\pi(T/\rho g)^{1/2}$. The solitons of this family are the small-amplitude extension of the finite-amplitude solitary waves calculated by Longuet-Higgins and VBD.

We find that all the soliton-like structures with single 'depression' are quite steep. A very large percentage of them fit quite well with theoretical profiles of solitary capillary–gravity waves of maximum slope of 0.917 to 0.59 (42.5°–30°). They are found at all wind speeds and some examples of these soliton-like waves are given in figures 3 and 4.

Figure 3(*a*) shows an image of wave surface gradient of a wave field of about 20 × 14 cm at a low wind speed of 5.9 m s^{-1}. There is an isolated short line of sharp gradient change in the upper middle part of the image. We take a surface profile vertically across it along section AA' as shown in figure 3(*a*) and plotted in figure 3(*b*).

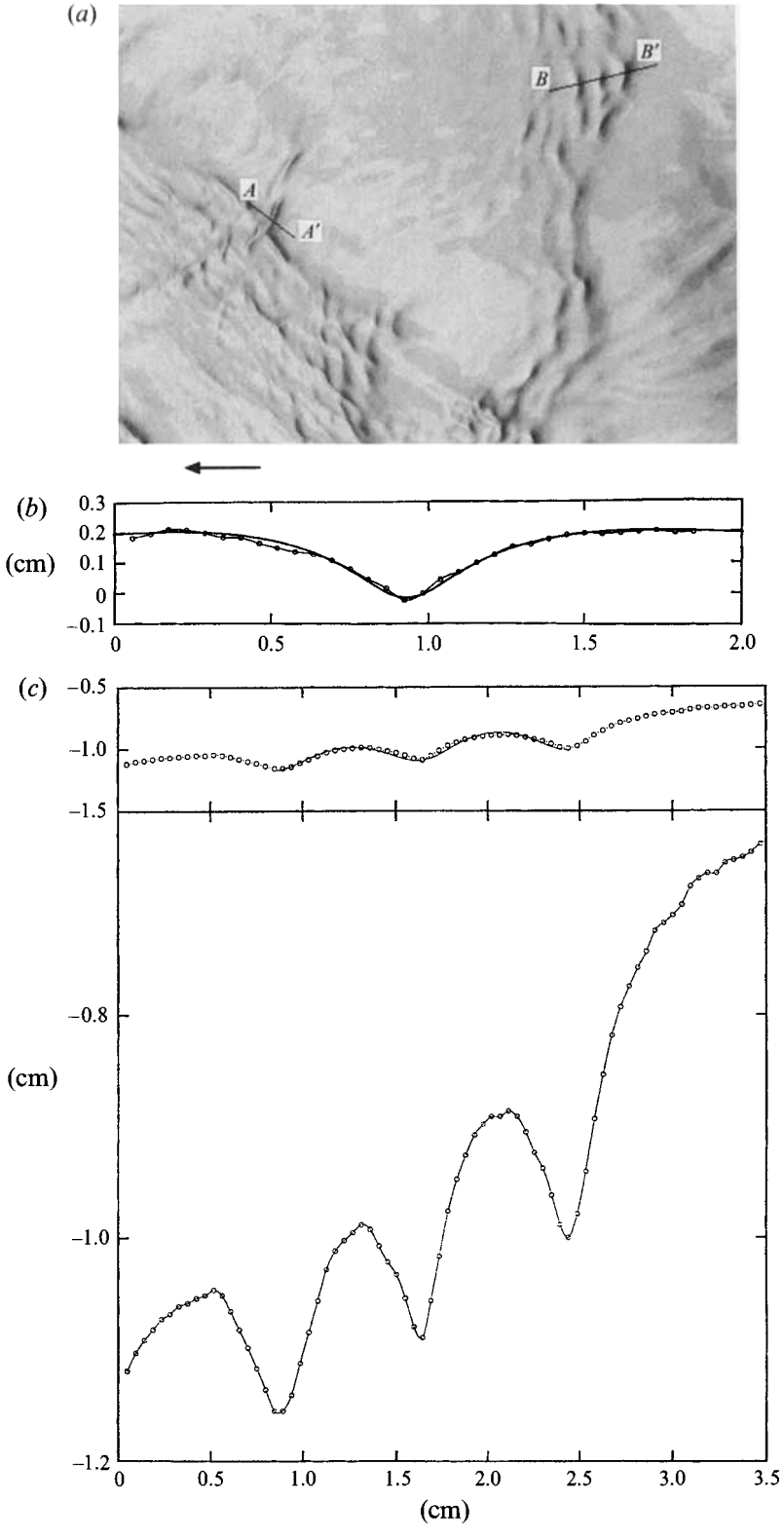

FIGURE 4. For caption see facing page.

This profile fits remarkably well with the profile of Longuet-Higgins' soliton of phase speed $1.25(gT/\rho)^{1/4}$, that is, appreciably slower than the minimum phase velocity $1.414(gT/\rho)^{1/4}$ for infinitesimal capillary–gravity waves. The whole trough length of the wave structure of about 1.2 cm is large in comparison with the width of the steep dip of less than 0.5 cm. It is also of interest to see if there is any similar isolated linear-structure of slope change with a small slope. We selected another feature near the bottom of figure 3(*a*) which is not as steep as the one chosen previously. Its vertical cross-section profile is taken along the line *BB'* as shown in figure 3(*a*) and plotted as figure 3(*c*). The maximum slope of this profile is much less than the maximum slope of a soliton of speed $1.30(gT/\rho)^{1/4}$ which has minimum slope in this single 'depression' soliton family. The multiple 'depressions' appeared in the profile. This profile has the feature of VBD solutions with the parameter α in between 0.225 and 0.295. Here the parameter α was introduced by VBD as a fourth-power of non-dimensionalized speed. Most of the single 'depression' soliton-like features we observed are very well matched against the theoretical solitons even when the shape of the crest is distorted. One explanation for the distortion could be the stretching by the background wave field while surface tension is dominant at steep wave troughs.

The gradient image of figure 4(*a*) was taken at a wind speed of 6.7 m s^{-1}. In the left part of this image there are several features showing sharp slope changes within a group propagating toward the upper left-hand corner of the image and another group towards the lower left corner. A profile is taken along section *AA'* plotted in figure 4(*b*). This profile matches the profile of a soliton of speed $1.30(gT/\rho)^{1/4}$ very closely. The group propagating to the upper left-hand corner seems to be cut into pieces from a long trough soliton when it passes through the longitudinal disturbances of the wave group propagating towards the lower left-hand corner. It is not yet known whether capillary–gravity solitary waves become unstable to the disturbance in the third dimension. The instability hypothesis made here is based on our observations that the lengthscale of troughs of the most soliton-like structures is around a few centimetres. The lengths of the steepest parasitic waves are in the order of 1 cm or less. In the upper right-hand corner of figure 4(*a*), there are three nearly parallel sharp slope changes very nearly equally spaced. A surface profile along line *BB'* is plotted as figure 4(*c*). We fit the profile with Crapper's pure capillary waves which has an analytical solution for each reproduction. The fit is good.

Some of solitary wave profiles observed match the analytical profile very well at the trough but not at the crest. We match the profiles in the troughs because they provide the sharpest curvature where surface tension force is the strongest. The flattened crests can be easily altered by the action of the background wave field. Most of the soliton-like structures in our data can be fitted in the trough portion very well, while some of their crests can be fitted well, but some cannot. It is not frequent to observe a soliton-like structure with a very long trough in our wind wave images. It is noted here that, comparing to other waveforms, these soliton-like structures are not frequent events so that it is not expected to be an important feature in the wave spectrum.

FIGURE 4. A wind wave field with soliton-like structures at a wind speed of 6.7 m s^{-1}. (Wave field of 20 × 14 cm). (*a*) Gradient image of short wave field. (*b*) Waveform profile along section *AA'*, the measured curve with circles matches with solitary waveform of phase speed of $1.30(gT/\rho)^{1/4}$. (*c*) Waveform profile of section *BB'*, the measured curve with circles matches up against Crapper capillary waves of slope 0.175, and its replot with a vertical to horizontal scale ratio of about 6 to 1.

4.3. *Asymmetry of short wind waves*

The short water wave forms derived from the irrotational theory are all symmetrical about the crest. A uniform shear by itself may not induce asymmetry in the surface profile (Simmen & Saffman 1985). However, under our experimental condition of wind waves, it is observed that the axis of symmetry of the short-wave troughs is tilted, in the sense of a flagpole bent by the wind. This tilt can be seen clearly by plotting short-wave profiles with a large exaggeration of vertical scaling of 6 to 1 as in figure 4(*c*). The non-symmetrical feature is clear on this plot. On the whole, the waveform changes slightly (compared to the slope of waves) for waves with slopes within the range of our measurements. The early observations of Schooley (1958) also showed this tilting phenomenon for the profiles of short wind waves at the glass sidewall of a tank. The effect of the sidewall is not certain. Since our profiles are away from the boundary of sidewalls, there is no friction stress from walls. The cause of the asymmetry could be a mutual result of forcing and dissipation. The structures of a viscous boundary layer of wind-drift shear can be very complicated. The extensive measurement of this wind-drift has not yet been made owing to the technical difficulties. There are virtually no theoretical explanations for this high-order tilting phenomenon yet. Since the asymmetry of short wind waves is small, the potential flow assumption may still be acceptable for simplifying analysis of these waves.

4.4. *Capillary blockage*

In the very short fetch laboratory condition where dominant gravity waves are short, steep and relatively long lived, an interesting phenomenon proposed by Phillips (1981) occurs. This is capillary blockage in which short dispersive waves are unable to propagate past the dominant wave crest. Any such short wind wave components that may be generated by the wind are therefore swept up by each long-wave crest. The cutoff wavelength of blocked waves depends on the wavelength and the slope of dominant gravity waves. Capillaries shorter than this cutoff are blocked. The steeper and shorter the dominant wave is, the longer the cutoff wavelength becomes. The amplitudes of successive dominant waves change as a wave group passes down the wave tank. When the slopes of dominant waves are high, freely travelling short wind waves are swept up and expelled from the upwind faces of the wave; only when the slope is low can short wind waves exist there. Since the parasitic capillaries travel steady with long gravity waves on the downwind faces, they are not subject to the blockage. Thus the phenomenon of capillary blockage is expected to be observed on the upwind faces of dominant wind waves.

Figure 2(*a*) is a good example of non-capillary blockage where the slope of a dominant background wave is very small and there are many short-wave features of irregular pattern on the upwind face of the background long wave. The short waves on the upwind faces of long waves are random and less organized than parasitic waves. Their wave pattern bears a resemblance to a broad beam pattern of two-dimensional capillary waves as suggested by Chen & Saffman (1985). When the slopes of dominant waves are high enough but not breaking, short waves can be suppressed totally on upwind faces owing to the mechanism of capillary blockage. As we can see from figure 5(*a*), there are no short waves on the upwind faces of gravity waves at all. On the downwind face, the parasitic waves are well defined. The feature of capillary blockage also shows up in the wavenumber spectra of short wind waves (§3).

4.5. *Parasitic capillaries*

Parasitic capillaries are the dominant phenomenon of extremely short waves in the wind wave fields at least before the wind becomes extremely strong. The crests of a train of parasitic capillaries are parallel to the crests of the underlying long wave. The water surface profiles of parasitic capillary trains along sections in the gradient image of figure 5(*a*) are plotted in figures 5(*b*) and 5(*c*). Some of the profiles of steep parasitic capillary trains closely resemble the waveform suggested by Ebuchi *et al.* (1987) based on their observation of wind-waves seen through the glass sidewall of a wave channel. The wavelength of the parasitic capillary waves decreases from the crest of the long-wave crest towards the trough, and so do the slopes. The first sharp trough of the wavetrain can be very steep. An interesting experiment has been done by Koga (1982) on the generation of a capillary wavetrain by a water jet. According to a private communication between Koga and Ebuchi, these capillary trains are observed if there is a dip edge (sharp trough) at the beginning of each wavetrain. These current-induced capillary wavetrains are parasitic waves in the sense that they extract energy from the underlying water current with a speed variation.

Another important feature of parasitic capillaries we found is that the longest wavelength of each capillary wavetrain is at the most 1 cm, and typically about 0.6–0.7 cm. It will be shown (in §5) that there is a critical wavenumber of low limit for which parasitic waves can extract energy from the underlying gravity waves to compete with strong viscous dissipation. After capillaries are generated at the gravity wave crests owing to the excess surface tension force at the sharp crest, parasitic waves will die quickly by viscous dissipation before they grow up if they cannot continuously obtain an energy supply from gravity waves. This feature also shows up in the wavenumber spectra of short waves. In the wavenumber spectra of slope, there is a local maximum after the wavenumber of the longest parasitic waves.

A large fraction of observed parasitic capillaries are not collimated as well as the wave pattern shown in the previous example of figure 5. As the wind speed increases (even in the image of figure 5) they are not strictly one-dimensional. They have a certain directional spreading. There are at least two factors that can generate a poorly collimated beam of parasitic waves. First, the long wind waves on which parasitic waves ride do not all move in the direction of the mean wind. The crests of dominant long waves can be long or short, can cut across one another, and can be linear or curved. In order for parasitic waves to stay on the downwind faces of long waves, their propagation speeds have to be matched with the orbital velocity of long waves. The two-dimensionality of the downwind faces of long waves has a direct effect on the directionality of parasitic capillaries.

As is mentioned in the beginning of §4.1, the short gravity and capillary–gravity wave components of wavelengths of a few centimetres increase rapidly with increasing wind speeds. These short-wave components have a wide angular spreading. When they become steep, they can also generate parasitic capillaries. Figure 6 shows an example of parasitic capillaries on the short waves of a wavelength of about 5 cm. A surface profile of parasitic waves generated by short waves taken along the section in the gradient image is also plotted. In the wave elevation profile of figure 6(*b*), parasitic capillaries appear almost in troughs of these very short gravity waves. This is because the orbital velocity of very short gravity waves is small. The propagation speeds of parasitic capillaries can only match the orbital velocity near the troughs.

Even when the background long waves are horizontally one-dimensional, the ripple trains are subject to longitudinal modulation instabilities. In the experiment on

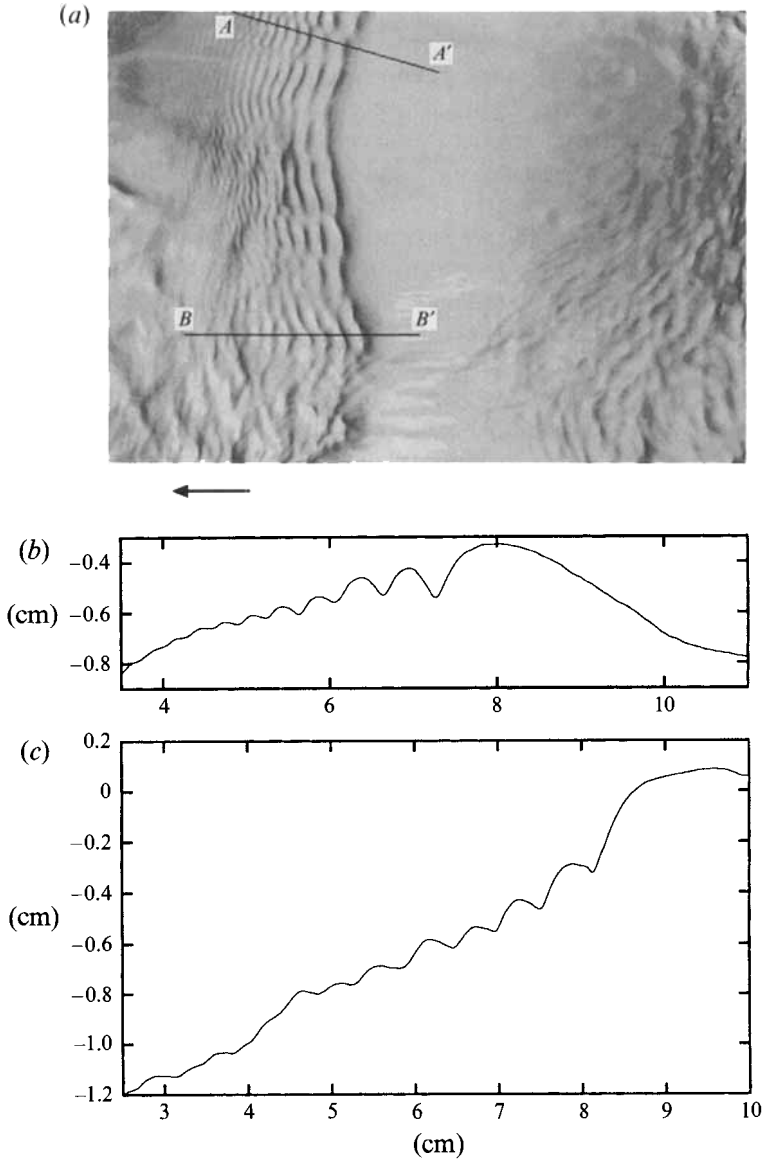

FIGURE 5. Parasitic wave pattern. (*a*) A gradient image of wind waves of windspeed 6.7 m s^{-1} (wave field of 20 × 14 cm). Profiles of parasitic wavetrains of sections $AA'(b)$, and $BB'(c)$.

mechanically generated ripples, Perlin & Hammak (1991) examined wave–wave resonant quartet interactions of the Benjamin–Feir type. Their experiments show that the evolution of horizontal one-dimensional wavetrains with appreciable amplitudes and frequencies exceeding 9.8 Hz is dominated by longitudinally modulational instabilities, that they ascribe to the Benjamin–Feir type. These quartet interactions remain dominant even for wavetrains that are unstable to resonant triad interactions ($f >$ 19.6 Hz), if selective amplification does not occur. The experiments further show that oblique perturbations with the same frequency as the underlying wavetrain, i.e. rhombus–quartet instabilities, amplify more rapidly and dominate all other modulational instabilities. The wave surface reflection images of longitudinally modulational

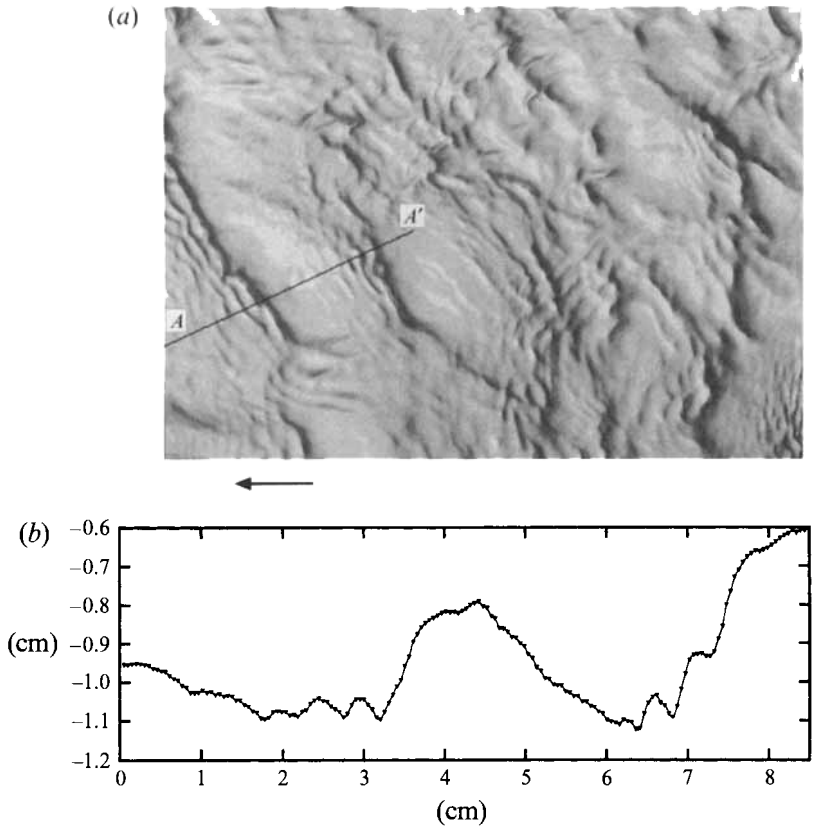

FIGURE 6. Parasitic wavetrains on very short gravity waves (5 cm). (*a*) The gradient image. Wind speed 9.7 m s^{-1} (wavefield of 20 × 14 cm). (*b*) Surface profile of section AA' of (*a*).

instabilities of their experiments show a two-dimensional wave pattern of striations in which alternating light and dark bands criss-cross the wave channel.

For the capillaries, the triad resonant selective condition cannot be satisfied unless the angle between two incident wavetrains is large (McGoldrick 1965). For the narrow-band parallel parasitic wavetrains, we can expect the longitudinally modulational instabilities of resonant quartet interactions of the Benjamin–Feir type rather than triads. One of our observational examples of longitudinal striations of slope alterations on parasitic wavetrains on forward faces of long waves are shown in figure 7(*a*). The longitudinal envelopes of parasitic wavetrains can also be seen from the wave surfaces image (figure 7*b*) reconstructed from the gradient data of the striations. As we can see from wave-surface images, the irregularity of amplitude that starts from the edge of the parasitic wavetrain, ends near the dominant wavecrests, becomes amplified a little toward the tail of the wavetrains, and extends beyond the tail of short wavetrains. Parasitic capillaries have moderate steepness in the wind wave field. The nonlinear instabilities are involved, and it is reasonable to assume that parasitic capillaries are only quasi-stable on the downwind faces of the background long gravity waves.

In contrast to the systematic feature of parasitic capillaries on the leeward face of the dominant wave, Ebuchi *et al.* (1987) found from their study of specular facets of wind waves in the laboratory that there are longitudinal specular facet streaks on the windward face of dominant waves as well. This feature is observed at low wind speed and when the dominant waves are quite uni-directional. They called this structure

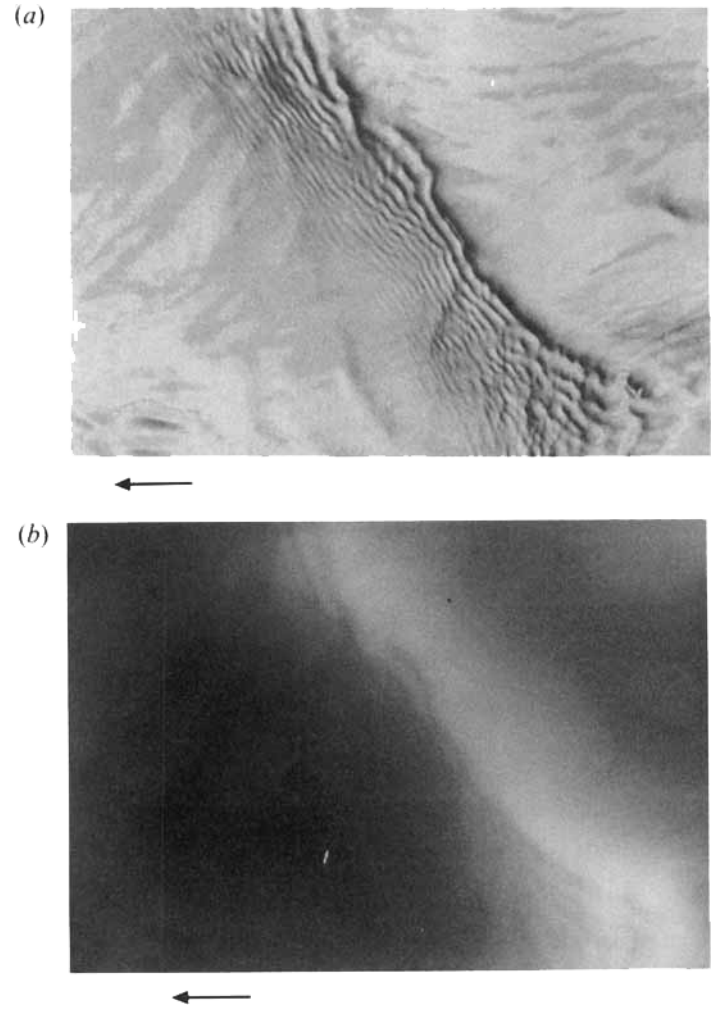

FIGURE 7. Scattering of parasitic wavetrains. (*a*) A gradient image of short wind waves at a wind speed of 5.9 m s^{-1} (wavefield of 20 × 14 cm). (*b*) The image of water surface elevation of (*a*).

'streamwise streaks'. We observed similar structures on some well-defined one-dimensional dominant long waves at low wind speed. An example can be seen in the gradient image of figure 7(*a*). The surface elevation variations due to this kind of structure are very small (figure 7*b*). However, we point out here that this feature is not frequent in our experiments at low wind speeds compared to the persistence in Ebuchi's experiments. A possible reason is that their channel is four times narrower than ours and their fetch is only about as half long as ours so that dominant gravity waves are shorter and much more unidirectional than ours. In figure 5(*a*), on the upper part of the upwind face of background wave there are no visible variations, but at the lower part there are several streamwise streaks.

A capillary roller and bore or a very strong vortical region on crests of steep gravity waves has been pointed out by Okuda *et al.* (1977) and also by Ebuchi *et al.* (1987). A generation mechanism of a positive feedback interaction between steep parasitic capillary waves and rollers has been proposed by Longuet-Higgins (1992). We have examined our image data for evidence of water surface fluctuations due to rollers at the

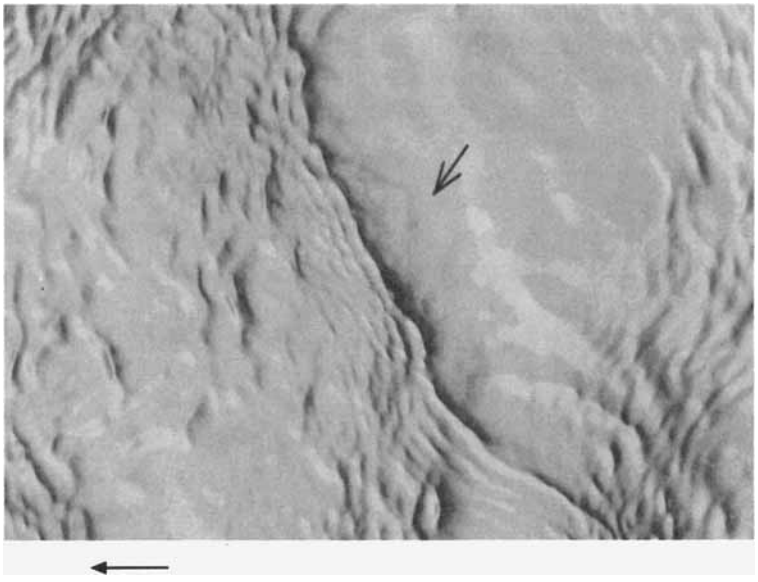

FIGURE 8. A gradient image of wind waves field of 20 × 14 cm at a wind speed of 6.7 m s^{-1}.

dominant wave crests region. Figure 8 shows very irregular variations of surface slopes immediately after the steep edge of parasitic wavetrains at the crest region. These irregular variations of surface slopes closely resemble bores created by gravity wave breaking. Longuet-Higgins (1992) suggested that 'streamwise streaks' may be surface manifestations of secondary vortices, as in 'windows' or Langmuir cells, the primary vortices, and that capillary rollers are caused by the capillaries themselves.

4.6. *Summary on short wind wave forms and structures*

Waveforms and spatial structures of short wind waves are discussed above. Many more examples of short-wave forms can be found in Zhang (1993). Before we focus further discussions on more theoretical analysis, the results can be summarized as follows:

1. Although short waves may have very steep slopes, very steep short waves that exceed 50° are quite limited in number. The slopes of short wind waves are generally small except for those solitary waves and for the first few wavelets of parasitic capillaries close to the crests of background long waves.
2. Waveforms resembling the Longuet-Higgins' solitons are observed.
3. High-order asymmetry of short wind waves is observed. The cause of asymmetry could be a mutual result of forcing and dissipation in the viscous wind-drift boundary layer.
4. It is found that the longest wavelength of parasitic waves is at most 1 cm.
5. All background gravity waves down to wavelength of 4 cm can generate parasitic wavetrains when their slope is large enough. At high wind speed, well-developed short gravity waves of a few centimetres can also generate parasitic short wavetrains.
6. Some profiles of parasitic short wavetrains observed agree with the one-dimensional pattern suggested by Ebuchi with a steep edge at the start of the wavetrain.
7. The longitudinal modulations of parasitic wavetrains are observed.
8. There are indications of a surface pattern on the backward faces of dominant long waves in which there exists a vortical region at the long-wave crests adjacent to the parasitic wavetrains.

9. Short wind waves observed can be divided into two general classes: parasitic capillaries and wind induced waves. In the laboratory, parasitic capillaries dominate short waves of wavelength less than 1 cm, while wind induced waves which appear less organized are subject to capillary blockage. Wind induced short waves increase much faster than parasitic capillaries as the wind grows.

10. The 'streamwise streaks' are much less frequently observed in our experiments.

5. The propagation of capillary surface waves on long gravity waves

As discussed in the above section, short waves are found to be enhanced on the downwind faces of long waves. These parasitic capillaries have a narrow angular distribution while short wind waves are less well organized. Locally the parasitic group has a well-defined wavelength though it can change with long-wave phase. In this section, we assume that short waves appear as a group with a locally narrow spectrum. We do not assume they are phase locked to the underlying long wave. Only the interaction between groups and underlying long waves is discussed so that its dynamics can be demonstrated. The interactions between the wave components in the group will be considered in a later section.

The variations in the wavelength and steepness of short gravity surface waves owing to the straining the surrounding water by the orbital velocity of the long waves is discussed by Longuet-Higgins (1987*a*) in detail. Following the same ideas, we shall briefly point out some interesting properties of parasitic capillary waves. For gravity waves, the phase speed decreases with decreasing wavelength, but the phase speed of capillary waves increases very rapidly with decreasing wavelength. Capillary waves are only sensitive to the water speed gradient in the long weaves and do not respond to the changes of apparent gravity caused by the up and down motions of the water surface of the long waves, but short gravity waves do. For capillaries moving in a steady state on a long wave, the two equations governing the capillaries are the wave crest and wave action conservation.

In a frame of reference moving with the phase speed C of the long wave, a group of short waves propagates against the long-wave orbital velocity q, at the local phase and group velocities c and c_g respectively (figure 9). We have:

$$k(c-q) = \omega_0 \tag{5.1}$$

where ω_0 is the apparent frequency of the short waves in the moving coordinate system, and is uniformly constant on all parts of the long wave. This steady assumption implies that the number of crests observed at different positions is the same for each short wavetrain. Here k is the wavenumber of short waves. The conservation of action is expressed by:

$$(c_g-q)\frac{E}{\omega} = \text{constant}. \tag{5.2}$$

Here ω is the intrinsic frequency with the dispersion relation $\omega^2 = gk + Tk^3$. E is the short-wave energy. It is noted that all these physical quantities of short waves, E, ω, k, c and c_g, are defined locally, and they are slowly changing functions of the underlying long-wave phase. This is because the length of the underlying energetic long wave is an order of magnitude longer than the short waves. We initially neglect the wave generation and dissipation due to wind forcing and viscosity. The change in apparent acceleration of gravity due to the up and down surface acceleration (about 20–35% of

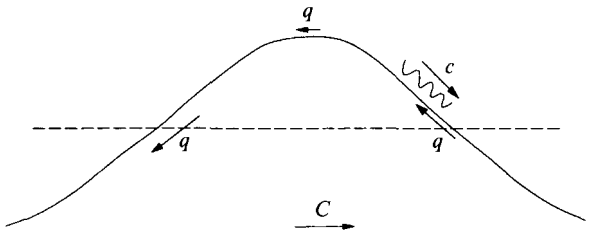

FIGURE 9. Short wave riding on a long wave travelling from left to right. The coordinate system is moving with the long wave so orbital velocities are all directed to the left.

g) of long waves is not included in the following discussion for simplicity. This can have some influence on gravity–capillary waves. Near the long-wave crest g is effectively reduced, which enhances the importance of surface tension.

Let us consider the steady state equation (5.1) a bit more. Let the wavenumber k be positive. Then the phases of the short waves are moving in the propagation direction of the underlying long wave when the constant, ω_0, is positive, and are moving in the opposite direction when it is negative. Taking a derivative with respect to the long-wave arclengths, s, in (5.1), and noting the identity

$$\frac{\partial c}{\partial s} = \frac{(c_g - c)}{k}\frac{\partial k}{\partial s},$$

we find that

$$\frac{\partial \ln(k)}{\partial s} = \frac{1}{(c_g - q)}\frac{\partial q}{\partial s}. \tag{5.3a}$$

Thus the fractional rate of wavenumber change is proportional to the local rate of change of the orbital velocity and inversely proportional to the difference in speed between the group velocity of the short waves and the orbital velocity of the long wave. If the group velocity of short waves is larger than the orbital velocity of the long wave, the wavelength of the short waves will increase as the orbital velocity decreases. The reverse is also true. Equation (5.3a) can be rewritten as:

$$\frac{\partial \ln(k)}{\partial q} = \frac{1}{(c_g - q)}. \tag{5.3b}$$

The fractional rate of wavenumber change with respect to the orbital velocity depends on the difference between the orbital speed of the long wave and the group speed (not the phase speed) of the short waves. If the net energy flux carried by short waves is to the right in figure 9, the wavelength is longer where the stream speed is smaller, reaching a maximum at the crest of the long wave. If the net energy flux is towards the left, the wavelength is longer where the stream speed is larger.

Let us suppose short waves are generated at the crest of the long wave and propagate downward to the trough to the right as parasitic capillary waves do. When the group velocity of short waves is larger than the orbital velocity, the short-wave group will appear on the forward face of the long wave. In this case the capillaries succeed in overcoming the opposition of the orbital velocity and propagate to the right against the stream. As the short-wave group propagates away from the long-wave crest, the orbital velocity increases. As a result of orbital straining, the wave-length of this wave shortens and the phase speed of the short wave approaches the orbital velocity of long waves so that parasitic capillaries are nearly stationary on the long wave. Their energy

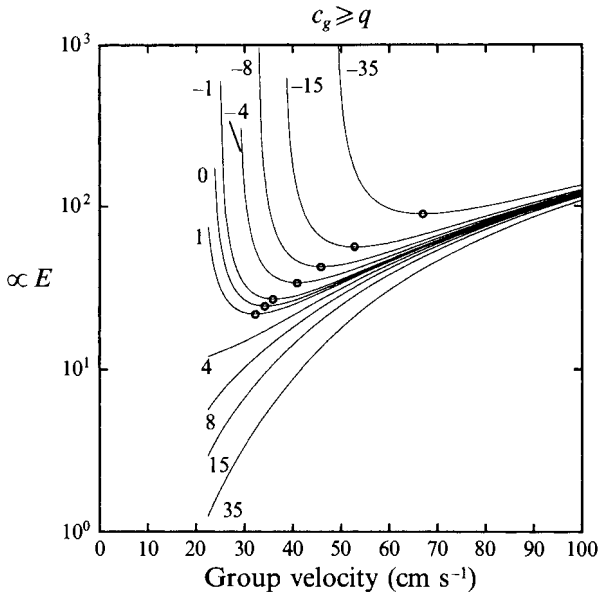

FIGURE 10. The energy of a group of capillary waves varies with its group velocity when the group velocity is larger than the orbital velocity of the underlying long wave. The number on each curve indicates the apparent frequency, $f_0 = \omega_0/2\pi$. For different values of ω_0 the energy decays rapidly as the group velocity increases if the group velocity of the short waves is very close to the underlying orbital velocity. When the wavenumber is initially larger than the critical wavenumber, $k_c(\omega_0)$, as indicated on each curve by a small circle, the energy of the short waves increases with increase of the group velocity. The plot is in a vertical relative scale (by setting constant of (5.2) to unit).

will change because of the action conservation. Equation (5.2) has been numerically calculated and is illustrated in figure 10 to show how the energy varies for various values of ω_0. The energy will increase if the initial wavenumber is larger than a certain critical value, $k_c(\omega_0)$, marked as a small circle on the curves of figure 10. For example, when the orbital velocity is equal to the phase speed of the short waves, the wavenumber has to be larger than $k_c(\omega_0 = 0) = 7$ rad cm^{-1} (wavelength less than 0.9 cm) in order to keep the wave energy growing. Recall here the fact that the dip in the wavenumber spectra shown in §3 extends up to about 7 rad cm^{-1} and the fact that the longest parasitic capillaries found are less than 1 cm (§4). As we can see from action conservation equation (5.2), when the group velocity of short waves is close to the orbital velocity of long waves, the short-wave energy becomes more sensitive to a change in orbital velocity than to a change of its frequency (we call it wave-current resonance type of instability). When the difference in speed is not very small for parasitic capillaries, increasing of short-wave energy will be determined largely by a change of the short-wave frequency owing to straining. The critical wavenumber depends on the speed difference between the short-wave phase speed and the orbital velocity of the underlying long wave, in other words, the apparent frequency ω_0. For a nearly stationary short wavetrain on the forward face of the long wave, the speed differences have to be very small. Parasitic short waves with wavenumbers much less than 7 rad cm^{-1} will decay rapidly and are unlikely to be observed.

For very short capillaries, the viscous dissipation becomes increasingly important. The rate of viscous energy dissipation is proportional to the square of the wavenumber. Waves pushed into higher wavenumber will suffer viscous dissipation ever more rapidly and therefore their growth will reach a maximum and then they will die unless re-

energized. The character of the parasitic capillaries when wind is not very strong is thus the result of an initial impulse at the crest of the long wave and then a competition between the energy input from the long wave by orbital straining and viscous dissipation rather than the competition between the energy input from wind and viscous dissipation.

As a second case we consider a group of short waves carried from the crest to the left towards the rear face of the long wave. The group velocity of the short waves is initially less than the magnitude of the orbital speed of the long waves or negative. As short waves move towards the trough, the orbital speed increases. Owing to the orbital stretch, the wavelength of the short waves increases so that there will be shorter waves near the crest and longer ones towards the trough, just the opposite condition of the parasitic capillary waves on the forward face of the long wave. Because of decreasing the wavenumber and increasing the different speed of group velocity and orbital velocity, the energy of short waves in this case is lost to the long waves from the action conservation equation (5.2). Adding viscous dissipation means that short waves cannot grow without an additional very strong external energy input such as wind forcing or energy derived from some other nonlinear interaction not considered here.

Finally, let us consider the case when short waves are generated somehow near the long-wave trough, for example by wind, and propagate towards the long-wave crests. When the short waves propagate to the right up the crest of the long wave, initially the magnitude of the orbital velocity is less than the group velocity. The wavelength of these short waves increases as they approach the crest so that their group speed decreases and approaches the orbital speed. This case has been discussed by Phillips (1981) and Shyu & Phillips (1990). According to (5.2) the energy of these waves either decays owing to orbital stretch or very quickly becomes very large so that they must be destroyed by breaking or reflection. On the other hand, if the short waves move to the left, Phillips adduces reasons why they are destroyed by passing over successive long-wave crests.

Short parasitic capillary waves on the forward face of a long wave are common in the laboratory wind-wave channel especially because gravity surface waves have a wavelength of less than 0.5 m. Such waves move slowly enough that capillaries can propagate downwind away from the crests. An important difference between crest and trough sources of capillary waves is that in the former case the phase speed is near orbital speed and orbital straining becomes important for parasitic capillary waves, while for the latter the group velocity approaches orbital speed and a resonance of wave-current type becomes important for the blocked waves.

The equation for the conservation of short-wave energy is

$$\frac{\partial}{\partial s}[E(c_g - q)] - S\frac{\partial q}{\partial s} = 0, \tag{5.4}$$

where S is the radiation stress, equal to three halves of the short-wave energy. Equation (5.4) essentially shows that the energy flux of the short waves is equal to the work done by the orbital velocity acting against the radiation stress of the capillaries. With (5.3*a*) for a steady state, we have

$$\frac{\partial[E(c_g - q)]}{[E(c_g - q)]} = \frac{3}{2}\frac{\partial k}{k} \quad \text{when} \quad c_g \neq q, \tag{5.5}$$

whence

$$[E(c_g - q)] \propto k^{3/2}, \tag{5.6}$$

which is a restatement of action conservation for the capillary waves. When short

waves are generated at the long-wave crests and propagate down towards the troughs, the forward face of long waves acts as an energy flux input to the short waves because k increases while the rear face acts as an energy sink. As a result parasitic waves are commonly found to be concentrated on the forward phase.

The energy term ignored in the energy conservation equation (5.4) is $-(\partial S/\partial s)q$ which is the work due to variation of radiation stress. This is the result of the assumption that the interference of short waves on long waves is negligible. It is necessary to emphasise that all the discussion above is based on the assumption of a steady state and irrotational flow.

6. Weak nonlinear interaction of capillary wind waves at high wavenumber

Another important factor of short-wave energy transfer is the interaction among different members of the short waves themselves. Here we neglect interactions with long waves to emphasize the physics of short-wave interactions, and defer to the next section an inclusive summary of forces and interactions.

Short waves are taken to be a quasi-Gaussian random process. Short wind waves can have a wide spectral band while parasitic capillaries locally have a narrow band. The wave field images and the distributions of the spectral angular spreading strongly support this assumption. The following discussion is based on the theory of irrotational and inviscid fluids and weak interactions, and it will certainly have to be modified when more is known about the thin surface shear flow induced by wind. The energy transfer among the different wavenumber components of short wind waves owing to wave–wave interactions is derived following the Hasselmann (1962) and Valenzuela & Laing (1972) with additional considerations. First, when parasitic waves have a very narrow angular distribution, the triad interaction conditions (McGoldrick 1965, 1970; Simmons 1969) cannot be satisfied, and quartet interactions should be taken into the consideration. Secondly, because short wind waves ride on large-amplitude, long gravity waves, the deviation of the water surface should be defined relative to the surface of the long waves rather than as a perturbation around the mean sea level. Accordingly, Holliday's method (1977) that allows perturbations around $z = \eta$ is adopted here instead of the usual perturbation around $z = 0$ that would converge too slowly. Detailed derivations can be found in Zhang (1993). Results needed for the next section are briefly as follows.

6.1. *Resonant conditions for triad and quartet interactions*

The resonant excitation condition for triad interactions

$$\omega^2(k) = (s_1\,\omega(k_1) + s_2\,\omega(k_2))^2, \quad \boldsymbol{k} = \boldsymbol{k}_1 + \boldsymbol{k}_2, \tag{6.1}$$

can be satisfied for gravity–capillary waves (McGoldrick 1965). Here $\boldsymbol{k}$, $\boldsymbol{k}_1$ and $\boldsymbol{k}_2$ are wavenumbers of triads and ω, ω_1 and ω_2 are their circular frequencies. The signs s_1 and s_2 can be independently plus or minus. A special case of (6.1) describes Wilton's ripples (Wilton 1915; Simmons 1969; McGoldrick 1970) in which an interaction is between a free wave and its free second harmonic propagate in the same direction. This occurs when the fundamental wavenumber is equal to $k_n = (g/2T)^{1/2} = k_m/\sqrt{2}$, a wavelength of about 2.4 cm for water. A striking feature of triads among pure capillary waves is that the angle between the wavenumber $\boldsymbol{k}_1, \boldsymbol{k}_2$ must be large and be limited in a small range (74°–83°) (McGoldrick 1965). This prevents the interaction of triads when the wave spectrum has a narrow angular distribution. In this case quartet interactions have to be taken into account.

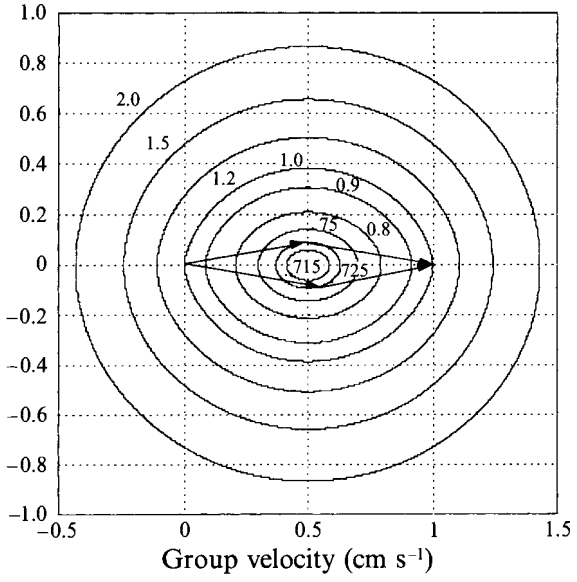

FIGURE 11. Wavenumber interaction chart for resonance of a quartet of capillary waves. As illustrated by the arrows, any two pairs of wave components on the same curves can be eligible for four interacting waves. The number on each curve indicates its γ value.

The resonant condition for quartet interactions among pure capillary waves is:

$$\boldsymbol{k}+\boldsymbol{k}_1 = \boldsymbol{k}_2+\boldsymbol{k}_3, \quad \omega(k)+\omega(k_1) = \omega(k_2)+\omega(k_3), \tag{6.2}$$

here the dispersion relation for capillary waves is

$$\omega^2(k_i) = Tk_i^3. \tag{6.3}$$

A diagram showing wavenumber selective relations of resonant capillary quartets is shown in figure 11 which follows the idea of Longuet-Higgins' gravity interaction chart. Any two pairs of vector wavenumbers joining two points on a curve as illustrated in the diagram can be eligible for four interacting waves. The curves are derived by letting

$$\boldsymbol{k}_1+\boldsymbol{k}_2 = \boldsymbol{k}_3+\boldsymbol{k}_4 = \boldsymbol{k}, \tag{6.4}$$

$$k_1^{3/2}+k_2^{3/2} = k_3^{3/2}+k_4^{3/2} = \gamma k^{3/2}, \tag{6.5}$$

with different γ values. Wavenumbers are normalized by setting $k = 1$. It can be seen from the diagram that two pairs of wave components can have both small directional differences and small wavelength differences.

6.2. *The rate of energy exchanges among wave components*

Let $F(\boldsymbol{k})$ be the energy spectrum of short waves divided by water density. At the lowest order, the relation to the wave elevation spectrum, $\Psi(\boldsymbol{k})$, is:

$$F(\boldsymbol{k}) = \tfrac{1}{2}k\,|c(\boldsymbol{k})|^2\Psi(\boldsymbol{k}) \tag{6.6}$$

where c is the short-wave phase speed. For a homogeneous, stationary Gaussian process, $F(\boldsymbol{k})$ does not change with time and completely determines the surface statistics in the linear approximation. We assume the short-wave field to be locally homogeneous, weak nonlinear, quasi-stationary Gaussian, with the lowest order assumed stationary and Gaussian. The non-stationary part of the energy densities

being of higher orders can be expressed by $F(\boldsymbol{k})$ through a perturbation expansion. The exchange of wave energy among different wave components is through redistribution of the non-stationary higher-order parts of the energy density. The changing part of energy density gives the energy transfer between different wavenumber components. The rate of energy spectrum change with time can be represented as a 'collision integral'. Here, for the purposes of discussion, only an order magnitude is needed. For triad interactions:

$$\frac{\partial F(\boldsymbol{k})}{\partial t} \propto k^5 \omega^{-1} F^2(\boldsymbol{k}), \tag{6.7}$$

and for quartet interactions:

$$\frac{\partial F(\boldsymbol{k})}{\partial t} \propto k^{10} \omega^{-3} F^3(\boldsymbol{k}). \tag{6.8}$$

Though the order of magnitude of the results are the same for both $z = 0$ and $z = \eta$ perturbations, the convergence range of $z = \eta$ perturbation is much faster than that of $z = 0$ perturbation.

7. The statistic equilibrium of short wind waves

In the two sections above, energy exchanges among wind wavenumber components within a group of short waves and between such a group and the underlying long wave are discussed separately in a qualitative sense with emphasise on the basic dynamics. An accurate and complete description involving all the forcing, interaction and dissipation processes is beyond our present ability to evaluate and would be very complicated. In the present circumstances we are justified only in making rough estimates of the magnitude of the various mechanisms, and relating them to observations of the slope spectrum. The total energy balance of short waves will be discussed in terms of the equilibrium spectrum. The statistical equilibrium spectrum represents the structure of the wave state when the forcing, dissipation and redistribution by nonlinear interaction are balanced. Following Phillips (1985), this can be described by the conservation of action spectral density:

$$\frac{\mathrm{d}N(\boldsymbol{k})}{\mathrm{d}t} = \frac{\partial N(\boldsymbol{k})}{\partial t} + (\boldsymbol{c}_g + \boldsymbol{U}) \cdot \nabla N(\boldsymbol{k}) = -\nabla_k \cdot \boldsymbol{T}(\boldsymbol{k}) + S_w + S_p - D = 0, \tag{7.1}$$

where $N(\boldsymbol{k})$ is the action spectral density and:

$$N(\boldsymbol{k}) = \frac{F(\boldsymbol{k})}{\omega} \tag{7.2}$$

in terms of the energy spectrum $F(\boldsymbol{k})$.

$\nabla_k \cdot \boldsymbol{T}(\boldsymbol{k})$ is the spectral flux of action owing to nonlinear wave–wave interaction. S_w is the input rate of wave action density from the wind. S_p denotes the input of short-wave action from long waves to form parasitic waves. D represents the total rate of all kinds of dissipation including wave breaking, viscous dissipation and suppression of short waves by surface-drift. The sources and sinks are all functions of energy density spectrum.

The nonlinear wave interaction flux term in the action conservation equation is dependent on the rate of change of $N(\boldsymbol{k})$ with respect to time:

$$-\nabla_k \cdot T(\boldsymbol{k}) = \frac{\partial}{\partial t} N(\boldsymbol{k}) = \frac{\partial}{\partial t} \frac{F(\boldsymbol{k})}{\omega}. \tag{7.3}$$

We have seen in §6 that there are two cases. First, for the case of capillary–gravity waves near the wavenumber k_m, triad interactions are dominant and:

$$-\nabla_k \cdot \boldsymbol{T}(\boldsymbol{k}) \propto k^5 \omega^{-2} F^2(\boldsymbol{k}). \tag{7.4}$$

Secondly, for the case of capillary waves with a narrow angular distribution, from (6.8):

$$-\nabla_k \cdot \boldsymbol{T}(\boldsymbol{k}) \propto k^{10} \omega^{-4} F^3(\boldsymbol{k}). \tag{7.5}$$

An estimate by Townsend (1972) and Plant (1982) for the wind input source term in the equation for the action conservation of short waves has the form:

$$S_w = m\left(\frac{u_*}{c}\right)^2 f(\theta)\, F(\boldsymbol{k}), \tag{7.6}$$

where c is the short-wave phase speed. Phillips (1985) explained this equation in terms of the energy input from wind stress being proportional to the wave slope. Since $c = (Tk)^{1/2}$ for pure capillary waves, the rate of wind action input is proportional to the inverse of wavenumber.

The dissipation of action by viscosity can be expressed (Lamb 1932, art. 348) as:

$$-D_\nu = -4\nu k^2 \omega^{-1} F(\boldsymbol{k}). \tag{7.7}$$

It can be seen that the viscous dissipation is increasing with the square root of k. If wind forcing and viscous dissipation acted alone, the spectrum of short waves would have a cutoff wavenumber immediately beyond the point where these two terms are balanced. The cutoff would depend on wind speed u_*. This is not the case that we observed.

The input to wave action of parasitic waves on the forward face of long waves consists of the work done by long waves to change the slope and wavelength of short waves as discussed in an earlier section. In the case of capillary waves, it can be written as

$$S_p = \frac{\partial}{\partial s}\left(F(\boldsymbol{k})\frac{c_g - q}{\omega}\right) = \frac{1}{\omega}\left\{\frac{\partial}{\partial s}[F(\boldsymbol{k})(c_g - q)] - S(\boldsymbol{k})\frac{\partial q}{\partial s}\right\}, \tag{7.8}$$

where q is the orbital velocity of long waves, and s is the arc length of the gravity long waves.

It is clear that the energy density $F(\boldsymbol{k})$ of short waves is a slowly changing function of long-wave phase. Our measurements are snap shots of this process in a fixed reference frame. The measured spectrum $\overline{F(\boldsymbol{k})}$ can be viewed as the averaged energy density over all long-wave phases. It has been shown by Phillips (1981) using the principle of stationary phase that:

$$\overline{F(\boldsymbol{\kappa})} \propto \left.\frac{2F(\boldsymbol{k})}{\Lambda^2 \dfrac{\partial k}{\partial s}}\right|_{k=\kappa}, \tag{7.9a}$$

where Λ is the wavelength of long waves. The above expression becomes inaccurate when the wavenumber of the parasitic waves corresponds to the minimum (k about 7 rad cm^{-1}, see §5) near the long-wave crests, presenting a singularity. The method of stationary phase has to be modified, requiring both the first and second derivations of phase to vanish at a crest, whence:

$$\overline{F(\boldsymbol{\kappa})} \propto \left.F(\boldsymbol{k})\frac{2\pi}{\Lambda^2\left(-\dfrac{1}{2}\dfrac{\partial^2 k}{\partial s^2}\right)^{2/3}} Ai^2(z)\right|_{k=\kappa}, \tag{7.9b}$$

where $$z = (k-\kappa)\left[-\frac{1}{2}\frac{\partial^2 k}{\partial s^2}\right]^{1/3}.$$

When the wavenumber κ becomes less than the minimum wavenumber in the short-wave train, $z > 0$, the Airy function Ai decreases monotonically and exponentially.

There are many terms in the conservation equation. Since parasitic capillaries exist even without wind, we first discuss the spectral range when wind forcing is not important for simplicity, and afterward consider the range where viscous dissipation is not important. Finally, the asymptotic forms of the spectra at the two extreme ranges can be matched up since their power laws of wavenumber are not very different.

In the range where viscous dissipation is much larger than the wind input of wave action, one of the terms capable of balancing the strong viscous term at the high wavenumber is the input of action from long waves. We propose that the balance here is essentially that of the enhancement of short-wave groups through the mechanism (§5) of orbital straining balanced against viscous dissipation:

$$4\nu k^2\omega^{-1}F(\boldsymbol{k}) = \frac{\partial}{\partial s}\left(F(\boldsymbol{k})\frac{c_g - q}{\omega}\right). \tag{7.10}$$

Assuming that action density is proportion to the nth power of wavenumber and that the orbital velocity is in order of magnitude equal to the phase velocity of the short waves, $q \approx c$ (Longuet-Higgins 1963) (for capillaries $(c_g - q)/\omega \approx (c_g - c)/\omega = (c/2\omega) = (1/2k)$), we have:

$$\frac{\partial k}{\partial s} \propto \frac{4\nu}{T^{1/2}}k^{5/2}. \tag{7.11}$$

The rate of shortening of wavelengths of short waves through the orbital straining has to be large in order for short waves to stay. This is just a order of magnitude analysis. Actually, the rate of the orbital straining can be larger near the sharp crests of long waves and weaker near the flat troughs.

Short waves propagate very slowly on the forward face of the long waves at a speed nearly equal to the difference between the short-wave phase velocity and long-wave orbital velocity. This can give enough time for wave–wave interactions to take place among members of an irregular group of short waves so that energy can be pushed even further toward higher wavenumbers. If we further assume that rates of action density exchange among different wavenumbers owing to wave–wave interactions, orbital straining and viscous dissipation are all approximately of the same order, then we have a second balance equation, valid when the capillary waves are highly directional:

$$\frac{\partial}{\partial s}\left(F(\boldsymbol{k})\frac{c_g - q}{\omega}\right) \propto -\nabla_k \cdot \boldsymbol{T}(\boldsymbol{k}) = k^{10}\omega^{-4}F^3(\boldsymbol{k}), \tag{7.12}$$

and this leads to:

$$F(\boldsymbol{k}) \propto Tk^{-3}\left(\frac{\partial k}{\partial s}\right)^{1/2}. \tag{7.13}$$

Hence, for the phase-averaged energy density spectrum:

$$\overline{F(\boldsymbol{k})} \propto \frac{Tk^{-3}}{A^2\left(\dfrac{\partial k}{\partial s}\right)^{1/2}} = \frac{T^{5/4}}{2\nu^{1/2}A^2}k^{-17/4}. \tag{7.14}$$

At high wind speed, when the angular distribution of short waves is broad, triad interactions can begin to dominate over quartet interactions. Then the corresponding expression becomes:

$$\overline{F(\boldsymbol{k})} \propto \frac{Tk^{-4}}{A^2}. \tag{7.15}$$

Now let us consider the second case. When the wavenumber is not large, wind forcing will be greater than viscous dissipation, and we neglect the latter for simplicity. Here we propose that the balance is between the wind input and the wave–wave interactions. At the same time, radiation stresses of short waves are working against long waves and orbital straining. Thus:

$$mu_*^2 k^2 \omega^{-2} f(\theta) F(\boldsymbol{k}) = -\nabla_k \cdot \boldsymbol{T}(\boldsymbol{k}), \tag{7.16}$$

$$\frac{\partial}{\partial s}[F(\boldsymbol{k})(c_g - q)] - S(\boldsymbol{k})\frac{\partial q}{\partial s} = 0. \tag{7.17}$$

These two balances do not have to be of the same order. Orbital straining is not likely to be directly related to the local wind input. From the balance equation (7.17) and Longuet-Higgins' (1963) assumption that in order of magnitude $c = q$, for the parasitic short waves, we find

$$\frac{\partial k}{\partial s} \propto k\frac{\partial \ln q}{\partial s}, \quad \frac{\partial^2 k}{\partial s^2} \propto k\left[\left(\frac{\partial \ln q}{\partial s}\right)^2 + \frac{\partial^2 \ln q}{\partial s^2}\right]. \tag{7.18}$$

Again we have not included changes of apparent g owing to long-wave surface vertical accelerations for simplicity. From the balance equation (7.16), we have

$$F(\boldsymbol{k}) \propto (mT)^{1/2} u_* k^{-5/2}, \quad F(\boldsymbol{k}) \propto mu_*^2 k^{-3}, \tag{7.19}$$

corresponding to quartet and triad interactions. Finally, we find that:

$$\overline{F(\boldsymbol{k})} \propto \frac{mu_*^2}{A^2 \dfrac{\partial \ln q}{\partial s}} k^{-4}, \tag{7.20}$$

for triad wave–wave interactions and:

$$\overline{F(\boldsymbol{k})} \propto \frac{(mT)^{1/2} u_*}{A^2 \dfrac{\partial \ln q}{\partial s}} k^{-3.5}, \tag{7.21}$$

for quartet wave–wave interactions.

On the forward face near the crests of long waves where the velocity of a short-wave train and the long-wave orbital velocity are very close, short waves will break or be reflected. In order for them to grow, their wavenumbers have to be greater than a critical wavenumber of about 7 rad cm^{-1}. Short waves propagating towards the crest are blocked out (Phillips 1981). A decrease in the energy spectrum at smaller wavenumber is expected, and:

$$\overline{F(\boldsymbol{\kappa})} \propto \left.\frac{F(\boldsymbol{k})\, k^{-2/3}}{A^2\left\{-\dfrac{1}{2}\left[\left(\dfrac{\partial \ln q}{\partial s}\right)^2 + \dfrac{\partial^2 \ln q}{\partial s^2}\right]\right\}^{2/3}} Ai^2(z)\right|_{k=\kappa}. \tag{7.22}$$

8. Further discussions of our spectral model

The action dissipation by viscosity increases with wavenumber while the action input from wind decreases. The wavenumber value of the turning point occurs when the two action terms become equal to each other. Balancing between wind forcing and viscous dissipation, we find:

$$k_\nu = \left(\frac{m^2}{16\nu^2 T}\right)^{1/3} u_*^{4/3}, \tag{8.1}$$

where m is a non-dimensional number. A typical for wind stress $\tau = 1$ dyn cm^{-2}. The corresponding friction speed is $u_* \approx 30$ cm s^{-1}. Phillips (1985) gives m the value 0.04. With these values $k_\nu = 15.8$ rad cm^{-1}, corresponding to a wavelength $\lambda_\nu = 0.4$ cm. When the wavenumber is much larger than k_ν, or there is little wind, the energy density spectrum is described by (7.14) and (7.15) depending on the angular distribution. When the wavenumber is much smaller than k_ν, the energy density spectrum has the asymptotic form of (7.20) or (7.21), again depending on the angular distribution. The power law behaviour of these spectral forms does not differ greatly in steepness. For this reason, the turning point cannot be identified clearly from the observed spectra. The constants of these two spectral forms can be found by matching them up at this turning point k_ν. In general terms, this explains why there is no apparent wind viscous cutoff. In other words, the spectrum is extended well beyond k_ν by orbital straining. Finally, viscosity destroys all extremely short waves when it overcomes orbital straining and wave–wave interactions.

At the lower end of the wavenumber spectrum of parasitic waves near 7 rad cm^{-1}, the spectrum decays quickly. Slow wind-generated short waves are overtaken by long waves and are blocked when the long waves are steep and less than half a metre or so in wavelength. For example, Shyu & Phillips (1990) found that a dominant wave with wavelength of 30 cm and maximum slope, AK of 0.2, 0.3 or 0.4, destroys freely travelling wind waves shorter than those having wavelengths less than about 0.8, 1.5 or 3.5 cm (wavenumbers 7.9, 4.2 or 1.8 rad cm^{-1}, respectively) at the crest. For a wavelength of 50 cm and the slope as above, the shortest freely travelling wind waves have lengths of about 0.5, 1 or 2.2 cm (wavenumber 12.5, 6.1 or 2.8 rad cm^{-1}) at the crest. This combined effect produces a dip in the capillary–gravity range of the short-wave spectrum, which we regard as a capillary blockage dip caused by wave-current resonant type of instability. Certainly, the wave nonlinear instability could still be a factor in producing the dip.

When the wind speed is over 10 m s^{-1} in our tank, the wavelength of dominant gravity waves increases beyond half a metre, and both capillary blockage and parasitic waves are less pronounced so that the dip tends to be filled in. In the spectral data of Jähne & Riemer (1990) at a fetch of 90 m, there is no apparent dip. This may be because the wavelength of energetic gravity wave is much larger than half a metre, and short wind waves are free from the blockage. Parasitic waves still ride on well-developed short-harmonic gravity waves.

It has been shown that the wind-speed dependence of the spectrum changes, depending on whether triad or quartet wave–wave interactions are dominant. Considering wave–wave interactions, when the wavenumber is close to k_m, and where the dispersion curve is concave upward, triad interactions are expected to be strong, and the spectrum increases with the square of the wind speed. As the wavenumber of the interacting waves increases, quartet interactions among parasitic capillary waves become more important because the angular distribution of the interacting waves is

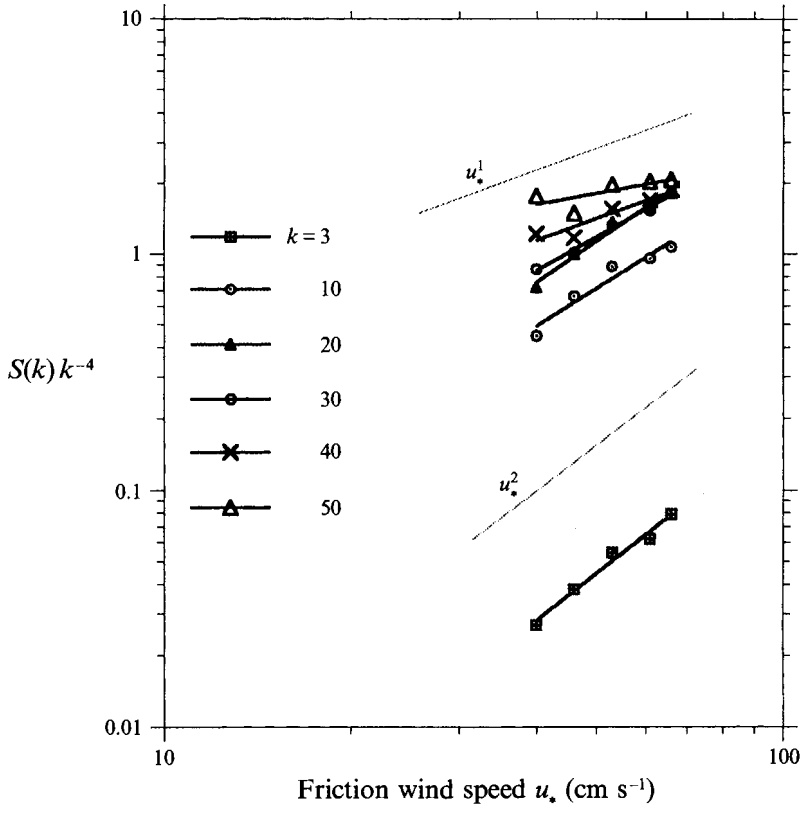

FIGURE 12. Dependence of spectral densities on the wind speed at wavenumber of 3, 10, 20, 30, 40 and 50 rad cm^{-1}.

small. We plot spectral values of slope at various wavenumbers against the friction wind speed in figure 12. There is evidence that the wind speed dependency changes from a square law to a linear relation as the wavenumber increases, in agreement with this proposal.

According to our analysis, long-wave orbital modulation has a dominant influence on the spectrum of short waves when short waves are unequally distributed on the forward and backward faces of long waves. It steepens the spectrum. The orbital straining for capillaries has a somewhat different effect to the orbital straining of short gravity waves. Short gravity waves are steeper and, unlike capillaries, shorter near the long-wave crests. The change of effective gravity acceleration has yet to be considered. For simplicity, we did not take this effect into account in our model. Though the spatial resolution of the measurements is low, the wavenumber spectra of short gravity waves measured by Banner, Jones & Trinder (1989) in the open sea are also steeper than predicted from Philips' equilibrium spectrum where the orbital modulation has not been taken into account.

In our current model, long waves are treated as having a uniform wavelength to simplify the calculations. A modified model that includes the randomness of long waves is needed to further improve our model, following along the lines of Longuet-Higgins (1987*b*), for example.

Shear in the wind-forced sublayer at the water surface and vortex formation at wave crests (Longuet-Higgins 1992) have not been included in our model. Some observed

phenomena of short waves (§4) cannot be interpreted owing to limitations of these and other assumptions, such as the assumed weakness of the nonlinear interactions. Fortunately, a large fraction of short waves are not extremely steep so that the present analysis may be regarded as an appropriate first-order approximation to the balance of action in short waves.

The work of this paper is part of my PhD thesis. I would like to express my deepest gratitude to my advisor, Charles S. Cox, for his guidance and help, for the original ideas as well as many features of this study, for the many years of support, and for the constant inspiration of his example.

REFERENCES

BANNER, M. L., JONES, I. S. F. & TRINDER, J. C. 1989 Wavenumber spectra of short gravity waves. *J. Fluid Mech.* **198**, 321–344.

CHEN, B. & SAFFMAN, P. G. 1985 Three-dimensional stability and bifurcation of capillary and gravity waves on deep water. *Stud. Appl. Math.* **72**, 125–147.

COX, C. S. 1958 Measurement of slopes of high-frequency wind waves. *J. Mar. Res.* **16** (3), 199–225.

CRAPPER, G. D. 1957 An exact solution for progressive capillary waves of arbitrary amplitude. *J. Fluid Mech.* **2**, 532–540.

EBUCHI, N., KAWAMURA, H. & TOBA, Y. 1987 Fine structure of laboratory wind-wave surfaces studies using an optical method. *Boundary-Layer Met.* **39**, 133–151.

HASSELMANN, K. 1962 On the nonlinear energy transfer in a gravity wave spectrum. Part 1. *J. Fluid Mech.* **12**, 481–500.

HASSELMANN, K. 1963 On the nonlinear energy transfer in a gravity wave spectrum. Part 2 and 3. *J. Fluid Mech.* **15**, 273–281; 385–398.

HASSELMANN, K., BARNETT, T. P., BOUNS, E. *et al.* 1973 Measurements of wind-wave growth and swell decay during the joint North Sea wave project. *Herausgegeben vom Deutschen Hydrographischen Institut*, A (8°), No. 12.

HOGAN, S. J. 1980 Some effects of surface tension on steep water waves. Part 2. *J. Fluid Mech.* **96**, 417–445.

HOLLIDAY, D. 1977 On nonlinear interactions in a spectrum of inviscid gravity–capillary surface waves. *J. Fluid Mech.* **83**, 737–749.

JÄHNE, B. 1989 Energy balance in small-scale waves – an experimental approach using optical measuring technique and image processing. In *Radar Scattering from Modulated Wind Waves.* (ed. G. Komen & W. Oost), pp. 105–120. Kluwer.

JÄHNE, B. & RIEMER, K. S. 1990 Two-dimensional wave number spectra of small-scale water surface waves. *J. Geophys. Res.* **95**, 11531–11546.

KAWAI, S. 1979 Generation of initial wavelets by instability of a coupled shear flow and their evolution to wind waves. *J. Fluid Mech.* **93**, 661–703.

KITAIGORODSKII, S. A. 1983 On the theory of the equilibrium range in the spectrum of wind-generated gravity waves. *J. Phys. Oceanogr.* **13**, 816–827.

KOGA, M. 1982 Bubble entrainment in breaking wind waves. *Tellus* **34**, 481–489.

LAMB, H. 1932 *Hydrodynamics.* Cambridge University Press.

LONGUET-HIGGINS, M. S. 1963 The generation of capillary waves by steep gravity waves. *J. Fluid Mech.* **16**, 139–159.

LONGUET-HIGGINS, M. S. 1987*a* The propagation of short surface waves on longer gravity waves. *J. Fluid Mech.* **177**, 293–306.

LONGUET-HIGGINS, M. S. 1987*b* A stochastic model of sea-surface roughness I. Wave crest. *Proc. R. Soc. Lond.* A **410**, 19–34.

LONGUET-HIGGINS, M. S. 1988 Limiting forms for capillary–gravity waves. *J. Fluid Mech.* **194**, 351–375.

LONGUET-HIGGINS, M. S. 1989 Capillary–gravity waves of solitary type on deep water. *J. Fluid Mech.* **200**, 451–478.

LONGUET-HIGGINS, M. S. 1992 Capillary rollers and bores. *J. Fluid Mech.* **240**, 659–679.

LONGUET-HIGGINS, M. S. 1993 Capillary–gravity waves of solitary type and envelope solitons on deep water. *J. Fluid Mech.* **252**, 703–711.

MCGOLDRICK, L. F. 1965 Resonant interactions among capillary–gravity waves. *J. Fluid Mech.* **21**, 305–331.

MCGOLDRICK, L. F. 1970 On Wilton's ripples: a special case of resonant interactions. *J. Fluid Mech.* **42**, 193–200.

MILES, J. W. 1962 On the generation of surface waves by shear flows. *J. Fluid Mech.* **13**, 433–448.

OKUDA, K., KAWAI, S. & TOBA, Y. 1977 Measurements of skin friction distribution along the surface of wind waves. *J. Oceanogr. Soc. Japan* **33**, 190–198.

PERLIN, M. & HAMMACK, J. 1991 Experiments on ripple instabilities. Part. 3. Resonant quartets of the Benjamin–Feir type. *J. Fluid Mech.* **229**, 229–268.

PHILLIPS, O. M. 1957 On the generation of waves by turbulent wind. *J. Fluid Mech.* **2**, 417–445.

PHILLIPS, O. M. 1958 The equilibrium range in the spectrum of wind-generated ocean waves. *J. Fluid Mech.* **4**, 426–434.

PHILLIPS, O. M. 1966 *The Dynamics of the Upper Ocean.* Cambridge University Press.

PHILLIPS, O. M. 1981 The dispersion of short wavelets in the presence of a dominant long wave. *J. Fluid Mech.* **107**, 465–485.

PHILLIPS, O. M. 1985 Spectral and statistical properties of the equilibrium range in wind-generated gravity waves. *J. Fluid Mech.* **156**, 505–531.

PLANT, W. J. 1982 A relationship between wind stress and wave slope. *J. Geophys. Res.* **87**, 1961–1967.

PLANT, W. J. & WRIGHT, J. W. 1977 Growth and equilibrium of short gravity waves in a wind–wave tank. *J. Fluid Mech.* **82**, 767–793.

SCHWARTZ, L. W. & VANDEN-BROECK, J. M. 1979 Numerical solution of the exact equations for capillary–gravity waves. *J. Fluid Mech.* **95**, 119–139.

SCHOOLEY, A. H. 1958 Profiles of wind-created water waves in the capillary–gravity transition region. *J. Mar. Res.* **16**, 100–108.

SHYU, J.-H. & PHILLIPS, O. M. 1990 Blockage of gravity and capillary waves by longer waves. *J. Fluid Mech.* **217**, 115–141.

SIMMEN, J. A. & SAFFMAN, P. G. 1985 Steady deep water waves on a linear shear current. *Stud. Appl. Maths* **62**, 95–111.

SIMMONS, W. F. 1969 A variational method for weak resonant wave interactions. *Proc. R. Soc. Lond.* A **309**, 551–575.

STOKES, G. G. 1980 Supplement to a paper on the theory of oscillatory waves. In *Mathematical and Physical Papers*, vol. 1, pp. 197–229. Cambridge University Press.

TOBA, Y. 1973 Local balance in the air–sea boundary processes. III. On the spectrum of wind waves. *J. Oceanogr. Soc. Japan* **29**, 209–220.

TOBA, Y. 1988 Similarity laws of the wind wave and coupling process of the air and water turbulent boundary layers. *Fluid Dyn. Res.* **2**, 263–279.

TOWNSEND, A. A. 1972 Flow in a deep turbulent boundary layer over a surface distorted by water waves. *J. Fluid Mech.* **55**, 719–735.

VALENZUELA, G. R. 1976 The growth of gravity–capillary waves in a coupled shear flow. *J. Fluid Mech.* **76**, 229–250.

VALENZUELA, G. R. & LAING, M. B. 1972 Nonlinear energy transfer in gravity–capillary wave spectra, with applications. *J. Fluid Mech.* **54**, 507–520.

VANDEN-BROECK, J. M. & DIAS, F. 1992 Gravity–capillary solitary waves in water of infinite depth and related free surface flows. *J. Fluid Mech.* **240**, 549–557.

WILTON, J. R. 1915 On ripples. *Phil. Mag.* **29** (6), 173.

WU, J. 1969 Laboratory studies of wind–wave interactions. *J. Fluid Mech.* **34**, 91–111.

ZHANG, X. 1993 A study of capillary and capillary–gravity wind waves: their structures, distributions, and energy balances. PhD thesis, SIO, University of California, San Diego.

ZHANG, X. 1994 Wavenumber spectrum of very short wind waves: an application of 2-D Slepian windows to the spectral estimation. *J. Atmos. Oceanic Tech.* **11**, part 2, 489–505.

ZHANG, X. & COX, C. S. 1991 A 2-D water surface detector for measuring wavenumber spectrum of very short wind waves. *EOS Trans. Am. Geophys. Union* **72**, 276.

ZHANG, X. & COX, C. S. 1994 Measuring the two dimensional structure of a wavy water surface optically: a surface gradient detector. *Exps Fluids* **17**, 225–237.